RSC Advances

PAPER

View Article Online
View Journal | View Issue

Cite this: *RSC Adv.*, 2021, **11**, 8940

A catalytic mechanism investigation of TiF_3 on hydriding/dehydriding properties of $Mg_{85}Cu_5Ni_{10}$ alloy

Yi Yin, *[ab] Yuanhong Qi,[a] Bo Li,[a] Hu Gu,[b] Jinghui Zhao,[b] Liqiang Ji,[b] Bo Zhang,[b] Zeming Yuan *[c] and Yanghuan Zhang [ac]

Received 4th December 2020
Accepted 23rd February 2021

DOI: 10.1039/d0ra10224e

rsc.li/rsc-advances

In this research, $Mg_{85}Cu_5Ni_{10}$–*x* wt% TiF_3 (*x* = 0, 2, 4, 6, 8) alloys were synthetized *via* ball milling and the catalytic mechanism of TiF_3 on hydrogenation and dehydrogenation of $Mg_{85}Cu_5Ni_{10}$ was studied. The microstructure, hydriding/dehydriding kinetics and thermodynamics of the alloys were discussed in detail. The TiF_3 catalyzed alloys have faster hydriding/dehydriding kinetics and lower thermodynamic stability. After hydrogen absorption and desorption, TiF_3 decomposes into TiH_2 and MgF_2. TiF_3, TiH_2 and MgF_2 promote to forming crystal defects, dislocations, grain boundaries and nanocrystals which are advantageous to speeding up the rate of hydrogen absorption and desorption. The dehydrogenation activation energy E_a(de) and dehydrogenation enthalpy ΔH(de) are reduced to 81.462 from 116.767 kJ mol^{-1} and 72.456 from 93.372 kJ mol^{-1} respectively by 6 wt% TiF_3. An appropriate amount of TiF_3 can improve the hydriding/dehydriding kinetics and thermodynamics of $Mg_{85}Cu_5Ni_{10}$.

Introduction

Energy is an important material basis for the survival and development of human society.[1,2] The rapid development of modern industry relies on the use of a large number of fossil fuels. Basically, our life and work are inseparable from fossil fuels. Nevertheless, all fossil fuels are non-renewable. In addition, environmental pollution and extreme climate change caused by fossil fuels make human beings face severe challenges. At present, all countries around the world are considering carbon emission reduction by reducing the use of fossil fuels and developing and using renewable energy. Therefore, the development of clean and efficient new energy has become an important issue for all countries, which is also an important guarantee to solve the energy crisis and human survival.[3–9] So far, there are many new energies that can replace traditional fossil fuels, including solar energy, wind energy, tidal energy, geothermal energy, nuclear energy, and hydrogen energy. Considering the factors of manufacture, transportation, safety, reliability, and environmental friendliness, hydrogen energy is one of the best choices. Since the 1990s, Japan, the United States, and some European countries have carried out hydrogen research and development plans. Toyota launched the second generation Mirai hydrogen fuel cell vehicle in 2019, marking that the fuel cell electric vehicle (FCEV) technology had entered a new stage. Nevertheless, there are still some important technical problems for the hydrogen energy system to fully implement and replace fossil fuels.[10–17] The first is cheap and mass-produced hydrogen production technology. The second is hydrogen storage and transportation. The third is to convert hydrogen into electricity and heat energy safely and efficiently in the application process. Among them, high-density, low-cost, safe, and high efficiency hydrogen storage technology are the key links of large-scale use of hydrogen energy.[18–20]

The advantages of the metal hydride hydrogen storage method are high hydrogen storage capacity, no need for high pressure and heat insulation container and good safety compared with the traditional gas and liquid hydrogen storage methods.[21,22] Among many metal hydride hydrogen storage materials, magnesium has a high reversible hydrogen storage capacity (7.6 wt%) which attracts many scholars' interest.[23–26] Besides, magnesium has a low price, abundant reserves, excellent heat resistance, good recyclability, and can form solid solution with other elements in equilibrium state. Unfortunately, MgH_2 has high thermal stability and needs high temperature to release hydrogen, and the rate of hydrogenation/dehydrogenation evolution is relatively slow, which limits its wide application. Many scholars have improved the poor dynamic and thermodynamic properties of magnesium based alloys by alloying, nanocrystallization and amorphization.[27] Generally, transition metal elements or rare earth elements are used to alloy with magnesium to ameliorate the hydrogen storage performance. Yuan *et al.*[28] synthetized Sm_5Mg_{41} and found that its initial dehydriding temperature was 270 °C

[a]*Central Iron and Steel Research Institute, Beijing 100081, China*
[b]*AT&M Environmental Engineering Technology Co. Ltd, Beijing 100081, China*
[c]*Key Laboratory of Integrated Exploitation of Baiyun Obo Multi-Metal Resources, Inner Mongolia University of Science and Technology, Baotou 014010, China. E-mail: iybeauty@126.com*

indicating that alloying with Sm reduced the thermal stability of hydrides. Some studies have shown that nanocrystallization can effectively ameliorate the kinetics of hydriding and dehydriding of magnesium. This is because nanoparticles and nanocrystals have many interfaces. The channel effect and surface effect introduced by nanocrystallization shorten the diffusion distance of hydrogen in the particles, reduce the time of hydrogenation reaction, and accelerate the rate of hydrogen absorption and desorption. Liu *et al.*[29] prepared Mg–6.9 at% Zn ultrafine particles *via* hydrogen plasma-metal reaction method. They demonstrated that the Mg–Zn nanoparticles could absorb 5.0 wt% H_2 at 300 °C in 20 min with 56.3 kJ mol^{-1} hydrogen absorption activation energy. Furthermore, amorphization by mechanical ball milling and vacuum rapid cooling technology also could improve hydrogen storage performance of magnesium. Zhang *et al.*[30] synthesized $(Mg_{24}Ni_{10}Cu_2)_{100-x}$-$Nd_x$ (x = 0, 5, 10, 15, 20) alloy through rapidly quenched under vacuum and found the alloy with amorphous structure had good electrochemical performance. Moreover, it is easy to add all kinds of catalysts during ball milling to prepare composite materials. As a catalyst, TiF_3 is often used to improve the hydrogen storage properties of magnesium based alloys. N. S. Mustafa and M. Ismail[31] investigated the effect of TiF_3 on the performance of $2NaAlH_4$–$Ca(BH_4)_2$ hydrogen storage properties and they found that the addition of TiF_3 reduced the onset decomposition temperature and the ab/desorption kinetic was also improved as compared to the undoped composite. N. N. Sulaiman[32] studied the H_2 storage properties of MgH_2/Cd–TiF_3 for the first time. The sorption properties of MgH_2/Cd were improved after adding with TiF_3. E_A for hydrogen desorption of doped composite was lowered to 107.0 kJ mol^{-1}. In addition, our study has proved that TiF_3 significantly improved the kinetics of hydrogen absorption and desorption of $Mg_{85}Zn_5Ni_{10}$ alloy, and reduced the dehydrogenation activation energy to 75.514 kJ mol^{-1}.[12] Therefore, we choose TiF_3 as catalyst to study the catalytic effect on the hydrogen storage properties of Mg–Cu–Ni alloy.

In this investigation, we prepared Mg–Cu–Ni alloy with TiF_3 catalyst to study the hydrogen storage properties and catalytic mechanism. The hydriding/dehydriding kinetics and thermodynamics were investigated in detail. The microstructure and characterization were tested and observed by XRD, SEM and HRTEM. The dehydrogenation activation energy, entropy and enthalpy were also fitted and calculated.

Experimental

First of all, the as-cast $Mg_{85}Cu_5Ni_{10}$ alloy was smelted. We used a vacuum induction furnace to prepare the as-cast $Mg_{85}Cu_5Ni_{10}$ alloy under 0.04 MPa He atmosphere as the protective gas. As a result of the high vapor pressure of Mg, it is very easy to burn and volatilize during smelting. According to smelting experience, more 10 wt% Mg was mixed in the smelting process in order to guarantee the designed composition of the as-cast $Mg_{85}Cu_5Ni_{10}$ alloy. Subsequently, the as-cast $Mg_{85}Cu_5Ni_{10}$ alloy was crushed into powders (particle size < 75 μm) mechanically. Finally, the $Mg_{85}Cu_5Ni_{10}$ powders and different contents of TiF_3 (produced by Thermo Fisher Technology (China) Co., Ltd) were mixed to ball mill by a planetary-type mill (Made by Instrument Factory of Nanjing University) under Ar atmosphere. The contents of TiF_3 were 0, 2, 4, 6 and 8 wt%. The ball to powder was 40 : 1. The milling speed was 350 rpm. In consideration of excess heating caused by milling, the mill process was rested for 1 h after every 1 h working. The total milling time was 5 h. All the block metal materials in this experiment were provided by China Iron & Steel Research Institute Group.

Hydrogen absorption/desorption kinetics of $Mg_{85}Cu_5Ni_{10}$–x wt% TiF_3 (x = 0, 2, 4, 6, 8) alloys were measured by a Sieverts-type apparatus (made by General Research Institute for Nonferrous Metals). At the beginning of tests, all the samples were absorbed and desorbed hydrogen for several cycles to activate completely. Hydrogenation was tested at a pressure of 3 MPa from 100 to 360 °C, and

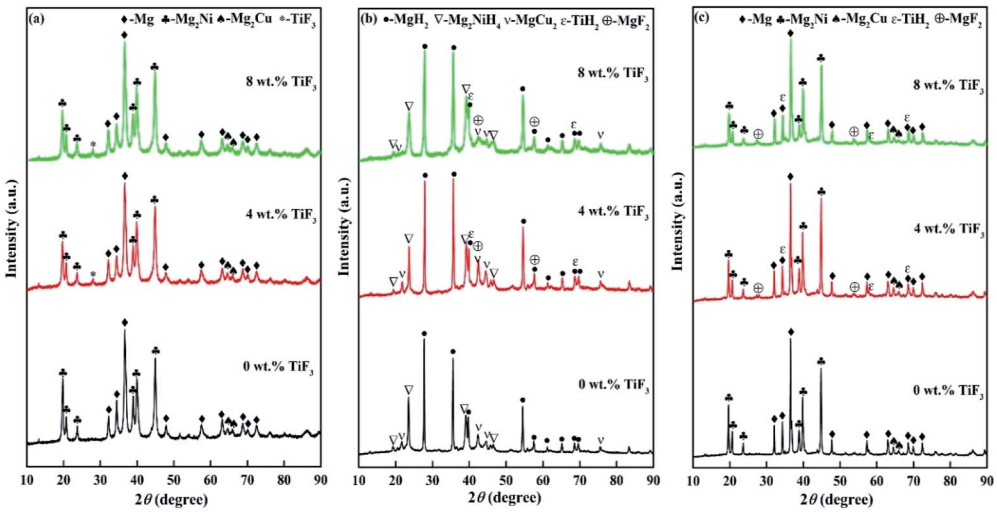

Fig. 1 XRD patterns of $Mg_{85}Cu_5Ni_{10}$–x wt% TiF_3 (x = 0, 4, 8) alloys: (a) before hydrogen absorption, (b) after hydrogen absorption, (c) after hydrogen desorption.

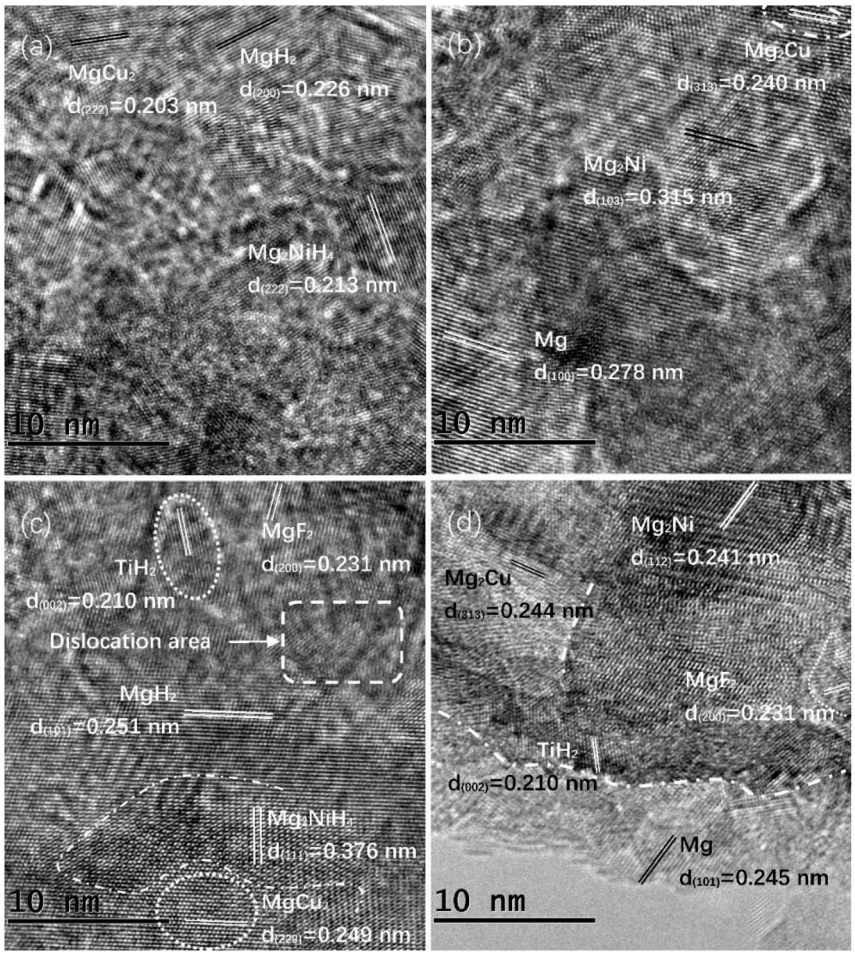

Fig. 2 HRTEM micrographs of $Mg_{85}Cu_5Ni_{10}$–0 wt% TiF_3 and $Mg_{85}Cu_5Ni_{10}$–4 wt% TiF_3 after hydrogen absorption (a) and (c), after hydrogen desorption (b) and (d).

dehydrogenation was tested at a pressure of 1×10^{-4} MPa from 240 to 360 °C. The purities of He, Ar and H_2 gases were 99.999% supplied by China Iron & Steel Research Institute Group.

Phase structures, morphologies and crystalline states of $Mg_{85}Cu_5Ni_{10}$–x wt% TiF_3 ($x = 0, 2, 4, 6, 8$) alloys were detected and observed by X-ray diffraction (XRD) (D/max/2400) using

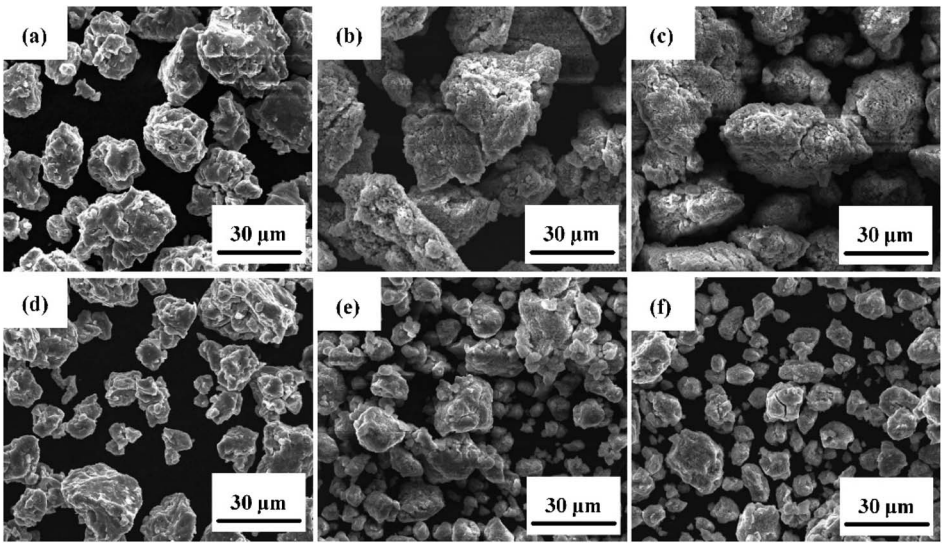

Fig. 3 SEM images of $Mg_{85}Cu_5Ni_{10}$–0 wt% TiF_3 and $Mg_{85}Cu_5Ni_{10}$–4 wt% TiF_3 after ball milling (a) and (d), after hydrogen absorption (b) and (e), after hydrogen desorption (c) and (f).

CuKα radiation with scanning rate of 2° min^{-1}, scanning electron microscopy (SEM) (QUANTA 400), scanning electron microscopy (SEM) (QUANTA 400) and high resolution transmission electron microscope (HRTEM) (JEM-2100F).

Results and discussion

Microstructural characteristics

X-ray diffraction (XRD) was used for clarifying the phase composition and hydrogenation and dehydrogenation reaction mechanism of $Mg_{85}Cu_5Ni_{10}$–x wt% TiF_3 (x = 0, 2, 4, 6, 8) alloys. Fig. 1 describes the XRD patterns of $Mg_{85}Cu_5Ni_{10}$–x wt% TiF_3 (x = 0, 4, 8) alloys after ball milling, hydrogenation and dehydrogenation. Because the patterns of $Mg_{85}Cu_5Ni_{10}$–x wt% TiF_3 (x = 2, 4, 6, 8) alloys are basically similar, in order to facilitate displaying and reading, Fig. 1 only shows the XRD patterns of $Mg_{85}Cu_5Ni_{10}$–x wt% TiF_3 (x = 0, 4, 8) alloys. As shown in Fig. 1(a), after ball milling, catalyst TiF_3 did not decompose. $Mg_{85}Cu_5Ni_{10}$–0 wt% TiF_3 consists of Mg, Mg_2Ni and Mg_2Cu. $Mg_{85}Cu_5Ni_{10}$–x wt% TiF_3 (x = 2, 4, 6, 8) alloys are composed of Mg, Mg_2Ni, Mg_2Cu and TiF_3. The little broadened diffraction peaks show that ball milling refines the alloy particles. According to Fig. 1(b), the Mg, Mg_2Ni and Mg_2Cu in $Mg_{85}Cu_5Ni_{10}$–0 wt% TiF_3 become into MgH_2, Mg_2NiH_4 and $MgCu_2$ respectively after hydriding. However, the TiF_3 decomposes into TiH_2 and MgF_2 in the catalyzed $Mg_{85}Cu_5Ni_{10}$ alloys after hydrogenation with the formation of MgH_2, Mg_2NiH_4 and $MgCu_2$. From Fig. 1(c), MgH_2, Mg_2NiH_4 and $MgCu_2$ change into Mg, Mg_2Ni and Mg_2Cu respectively after dehydriding, meanwhile, the TiH_2 and MgF_2 still exist in the alloys. It indicates that the thermodynamic properties of TiH_2 and MgF_2 are stable and do not decompose under the condition of dehydrogenation evolution in this experiment. On the basis of analysis above, the possible hydriding/dehydriding mechanism of $Mg_{85}Cu_5Ni_{10}$–x wt% TiF_3 (x = 0, 2, 4, 6, 8) alloys are:

$$Mg + H_2 \leftrightarrow MgH_2$$

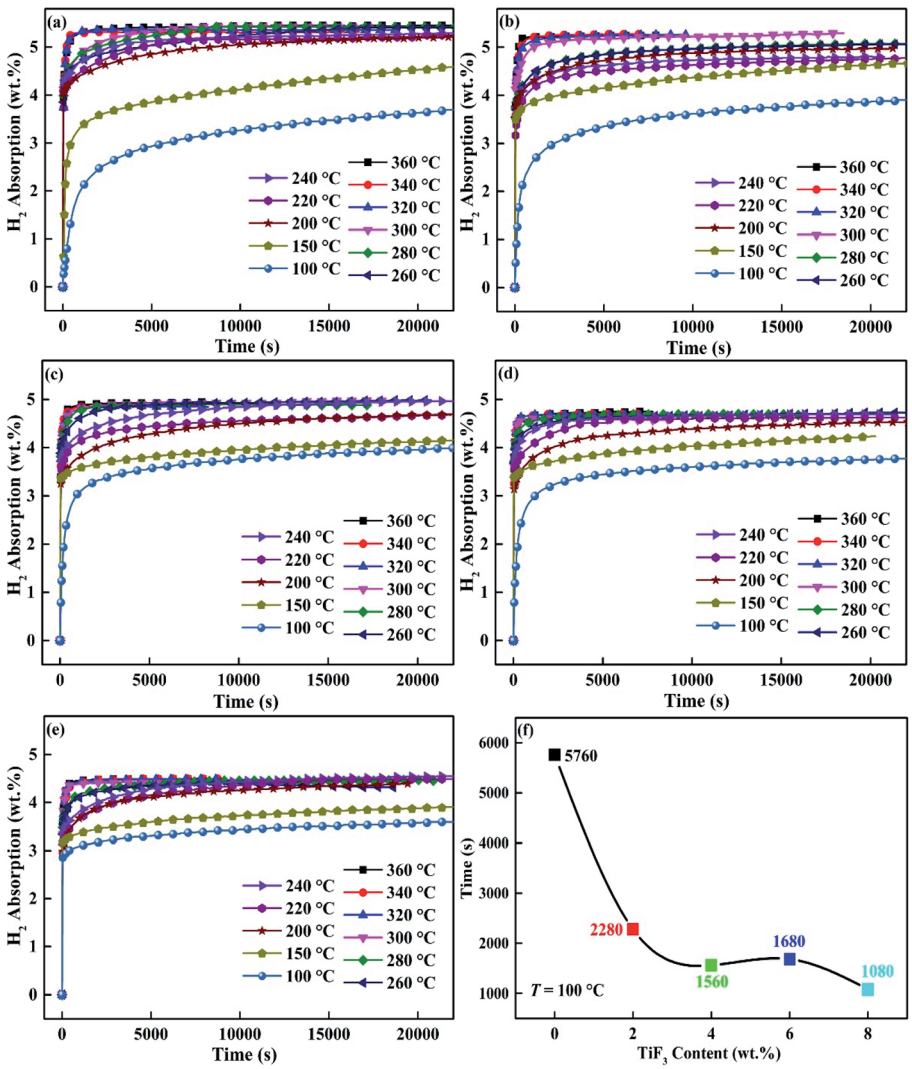

Fig. 4 Hydrogen absorption kinetic curves of $Mg_{85}Cu_5Ni_{10}$–x wt% TiF_3 (x = 2, 4, 6, 8) alloys at different temperatures: (a) x = 0; (b) x = 2; (c) x = 4; (d) x = 6; (e) x = 8 and the time required to absorb 3 wt% hydrogen at 100 °C (f).

$$Mg_2Ni + 2H_2 \leftrightarrow Mg_2NiH_4$$

$$2Mg_2Cu + 3H_2 \leftrightarrow MgCu_2 + 3MgH_2$$

$$2TiF_3 + 3Mg + 2H_2 \rightarrow 2TiH_2 + 3MgF_2.$$

High resolution transmission electron microscope (HRTEM) was selected to further study the phase transition and microstructure of $Mg_{85}Cu_5Ni_{10}$–x wt% TiF_3 (x = 0, 2, 4, 6, 8) alloys before and after hydriding and dehydriding. Fig. 2 shows the TEM images of $Mg_{85}Cu_5Ni_{10}$–0 wt% TiF_3 and $Mg_{85}Cu_5Ni_{10}$–4 wt% TiF_3 after hydrogenation and dehydrogenation. On the basis of Fig. 2(a) and (b), $Mg_{85}Cu_5Ni_{10}$–0 wt% TiF_3 consists of MgH_2, Mg_2NiH_4 and $MgCu_2$ after hydriding. After dehydriding, it contains Mg, Mg_2Ni and Mg_2Cu, which is consistent with the results of XRD analysis in the previous section. Instead, $Mg_{85}Cu_5Ni_{10}$–4 wt% TiF_3 is composed of MgH_2, Mg_2NiH_4, $MgCu_2$, TiH_2 and MgF_2 after hydrogenation indicating that the catalyst TiF_3 decomposes into TiH_2 and MgF_2 during hydriding process from Fig. 2(c). Meanwhile, according to Fig. 2(d), $Mg_{85}Cu_5Ni_{10}$–4 wt% TiF_3 contains Mg, Mg_2Ni, Mg_2Cu, TiH_2 and MgF_2 after dehydrogenation suggesting that TiH_2 and MgF_2 still exist in the alloy. The TEM image further proves that for $Mg_{85}Cu_5Ni_{10}$ alloy, the catalyst TiF_3 decomposes and forms stable TiH_2 and MgF_2 during the hydrogen absorption and desorption. Furthermore, we can observe the existence of crystal defects, dislocations, grain boundaries, nanocrystals and amorphous illustrating that after ball milling for 5 hours with catalyst TiF_3, the microstructure of $Mg_{85}Cu_5Ni_{10}$ alloy changes obviously after hydriding and dehydriding cycles. TiF_3 promotes the formation of nanocrystals on the surface of $Mg_{85}Cu_5Ni_{10}$ alloy and introduces high density grain boundaries.

Fig. 3 shows the SEM images of $Mg_{85}Cu_5Ni_{10}$–0 wt% TiF_3 and $Mg_{85}Cu_5Ni_{10}$–4 wt% TiF_3 after ball milling, after hydrogen absorption and after hydrogen desorption. From Fig. 3, the alloys particles present irregular spheres. After ball milling, the

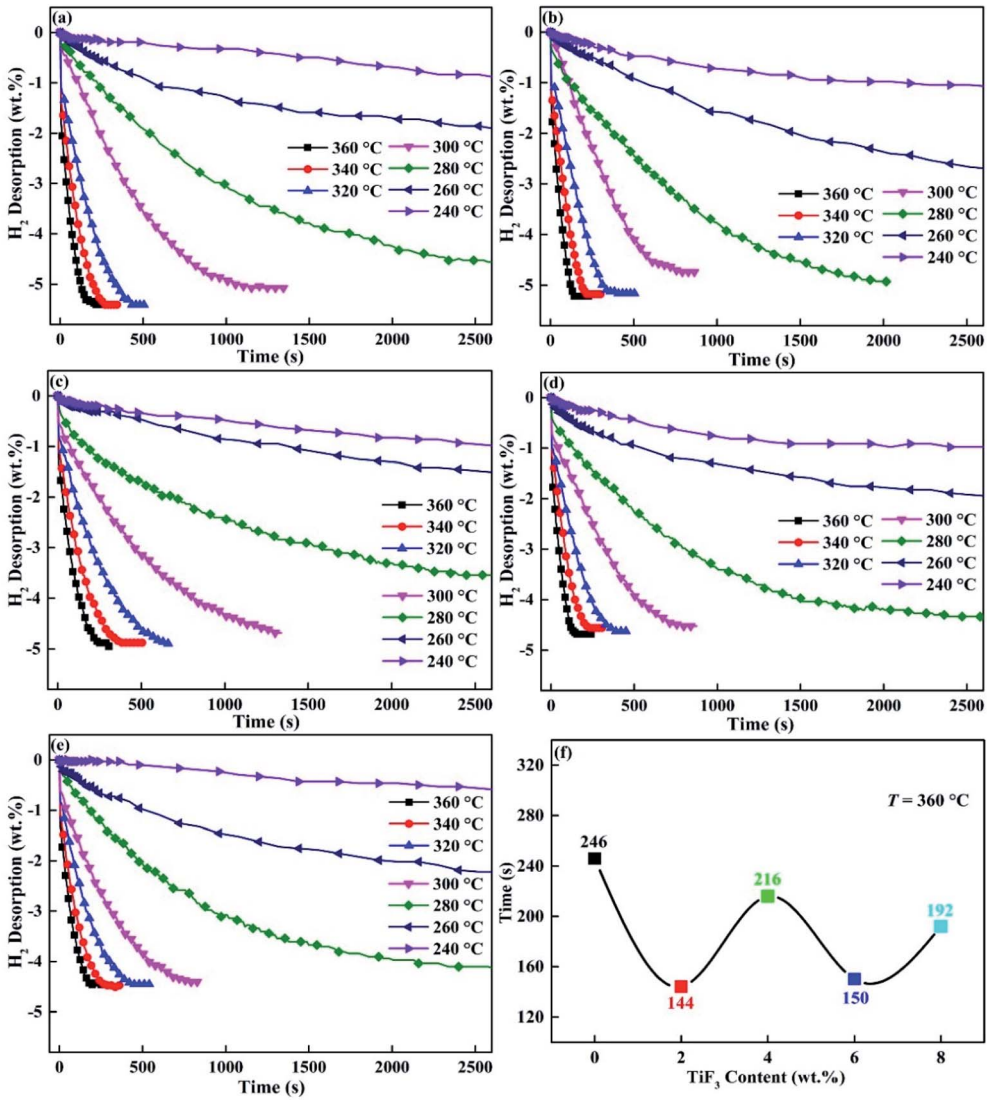

Fig. 5 Hydrogen desorption kinetic curves of $Mg_{85}Cu_5Ni_{10}$–x wt% TiF_3 (x = 2, 4, 6, 8) alloys at different temperatures: (a) x = 0; (b) x = 2; (c) x = 4; (d) x = 6; (e) x = 8 and the time required for complete dehydrogenation at 360 °C (f).

particle diameter is about 30 μm. However, $Mg_{85}Cu_5Ni_{10}$–0 wt% TiF_3 particles agglomerate, and $Mg_{85}Cu_5Ni_{10}$–4 wt% TiF_3 particles are pulverized after hydriding and dehydriding. It indicates that TiF_3 is helpful to refine alloy particles during hydriding and dehydriding cycles which is beneficial to increase the contact area of hydrogen absorption and desorption reaction. In addition, after the cycles of hydrogen absorption and desorption, some cracks appear on the surface of the particles. Our previous study has confirmed that these cracks contribute to accelerating the rate of hydrogen absorption and desorption.[12,27] In addition, it is worth noting that TiF_3 decomposes into TiH_2 and MgF_2 during hydriding and dehydriding process of $Mg_{85}Cu_5Ni_{10}$, while in our previously published work,[12] TiF_3 does not decompose in $Mg_{85}Zn_5Ni_{10}$. It may be due to fact that $MgZn_2$ is a stable phase in $Mg_{85}Zn_5Ni_{10}$ alloy while there is a transformation between Mg_2Cu and $MgCu_2$ in $Mg_{85}Cu_5Ni_{10}$ alloy during hydrogenation and dehydrogenation. The stable $MgZn_2$ and transformation between Mg_2Cu and $MgCu_2$ may explain the decomposition of TiF_3 in Mg–Cu–Ni alloy. There is a small amount of excess Mg appearing in the Mg_2Cu and $MgCu_2$ transformation process, making Ti and F reacting with Mg and H to form MgF_2 and TiH_2.

Kinetic properties of hydrogenation and dehydrogenation

In order to study the effect of TiF_3 on the kinetics of hydrogen absorption and desorption of $Mg_{85}Cu_5Ni_{10}$, the kinetics of hydriding and dehydriding of $Mg_{85}Cu_5Ni_{10}$–x wt% TiF_3 ($x = 0$, 2, 4, 6, 8) alloys was measured at different temperatures after fully activating. Fig. 4(a)–(e) describe the hydrogenation curves of $Mg_{85}Cu_5Ni_{10}$–x wt% TiF_3 ($x = 0$, 2, 4, 6, 8) alloys from 100 to 360 °C. All five alloys have very fast hydrogen absorption rates at high temperatures, and all of them can basically reach the saturation state in a short time on the basis of Fig. 4. However, with the decrease of hydrogen absorption temperature, the kinetic properties of the five alloys are gradually different. According to Fig. 4(a), $Mg_{85}Cu_5Ni_{10}$–0 wt% TiF_3 has a rapid hydrogen absorption rate when the temperature is higher than 320 °C. When the temperature is at the range of 300–200 °C, the hydrogen absorption rate and capacity of $Mg_{85}Cu_5Ni_{10}$–0 wt% TiF_3 decrease along with temperature decreasing. The hydrogen absorption speed and capacity of $Mg_{85}Cu_5Ni_{10}$–0 wt% TiF_3 decrease obviously when the temperature is lower 200 °C. However, the TiF_3 catalyzed alloys have faster hydrogen

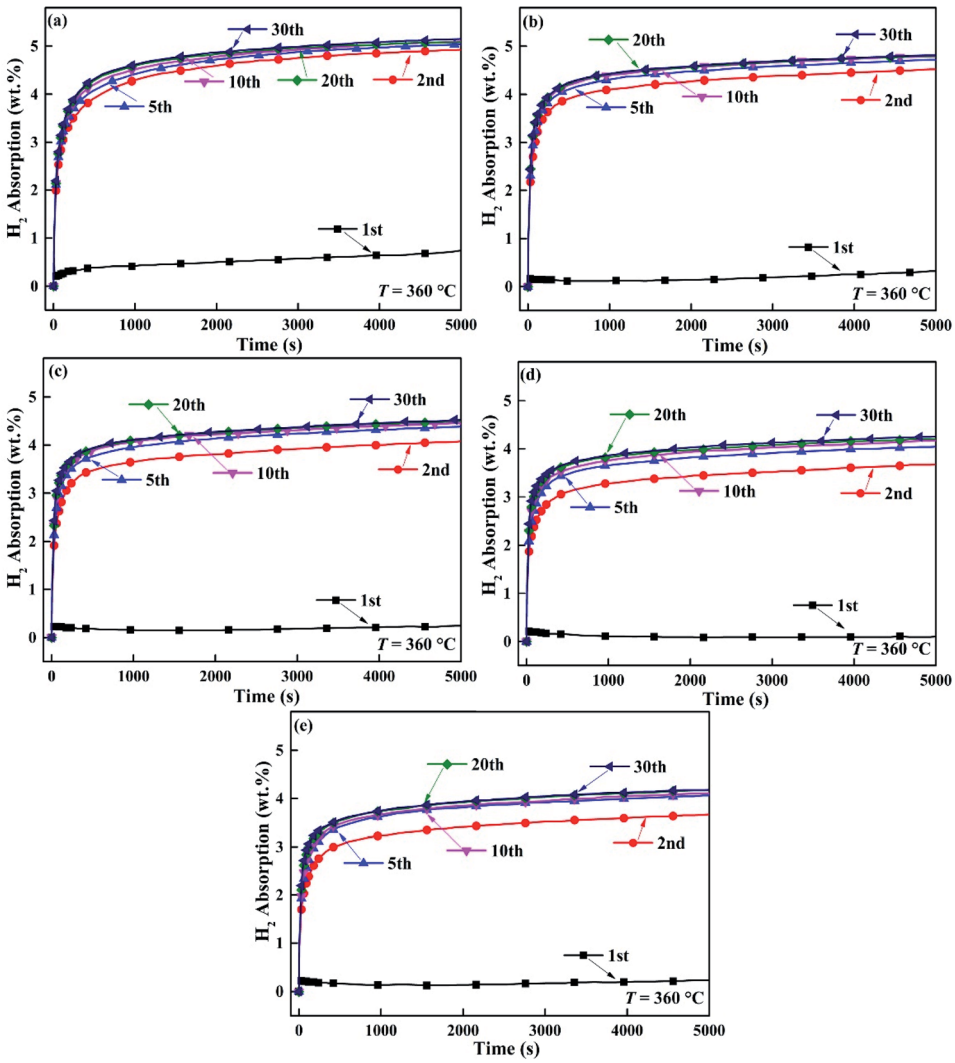

Fig. 6 Hydrogenation cycling curves of $Mg_{85}Cu_5Ni_{10}$–x wt% TiF_3 ($x = 2$, 4, 6, 8) alloys at 360 °C: (a) $x = 0$; (b) $x = 2$; (c) $x = 4$; (d) $x = 6$; (e) $x = 8$.

absorption rates when the temperature is lower than 300 °C. The results show that TiF_3 improves the hydrogen absorption kinetics of $Mg_{85}Cu_5Ni_{10}$ below 300 °C. The most intuitive embodiment is that the hydrogen absorption curves of the four TiF_3 catalyzed alloys at the range of 300–200 °C are closer to those above 300 °C. Fig. 4(f) shows the time required to absorb 3 wt% hydrogen of $Mg_{85}Cu_5Ni_{10}$–x wt% TiF_3 (x = 0, 2, 4, 6, 8) alloys at 100 °C. Obviously, the times required for the four alloys containing TiF_3 to absorb 3 wt% hydrogen are significantly shorter than that for $Mg_{85}Cu_5Ni_{10}$–0 wt% TiF_3 at 100 °C. It illustrates that TiF_3 significantly improves and increases the hydrogen absorption rate of $Mg_{85}Cu_5Ni_{10}$. However, due to the decomposition of TiF_3 and the formation of TiH_2 and MgF_2, the saturated hydriding capacities of the alloys also decrease.

Fig. 5 shows the dehydrogenation curves of $Mg_{85}Cu_5Ni_{10}$–x wt% TiF_3 (x = 0, 2, 4, 6, 8) alloys from 240 to 360 °C. As Fig. 5 describing, temperature affects the dehydrogenation performance of the alloys very much. $Mg_{85}Cu_5Ni_{10}$–x wt% TiF_3 (x = 0, 2, 4, 6, 8) alloys can complete all hydrogen release in 10 min with fast rate of dehydriding over 320 °C. When the dehydrogenation temperature is 360 °C, the time required for complete dehydrogenation is 246 s, 144 s, 216 s, 150 s and 192 s respectively (Fig. 5(f)). The dehydrogenation time increases with the decrease of dehydrogenation temperature. $Mg_{85}Cu_5Ni_{10}$–0 wt% TiF_3 can completely release hydrogen in 25 min, while the TiF_3 catalyzed alloys can completely dehydrogenate in 20 min at 300 °C. $Mg_{85}Cu_5Ni_{10}$–0 wt% TiF_3 only can release some hydrogen with more than 1 h, while the TiF_3 catalyzed alloys can completely dehydrogenate in 50 min at 280 °C. When the dehydrogenation temperature is below 280 °C, all of the five alloys show poor dehydrogenation performance, and it takes a long time for partial dehydrogenation. The above results and analysis show that the dehydrogenation performance of $Mg_{85}Cu_5Ni_{10}$ is obviously improved after TiF_3 catalyzing.

Hydrogenation and dehydrogenation cyclic stability

Fig. 6 and 7 express the hydrogenation and dehydrogenation cyclic stability curves of $Mg_{85}Cu_5Ni_{10}$–x wt% TiF_3 (x = 0, 2, 4, 6, 8) alloys at 360 °C. As shown in the images, there is nearly no change of hydrogen absorption and desorption capacities for $Mg_{85}Cu_5Ni_{10}$–x wt% TiF_3 (x = 0, 2, 4, 6, 8) alloys after 20 cycles.

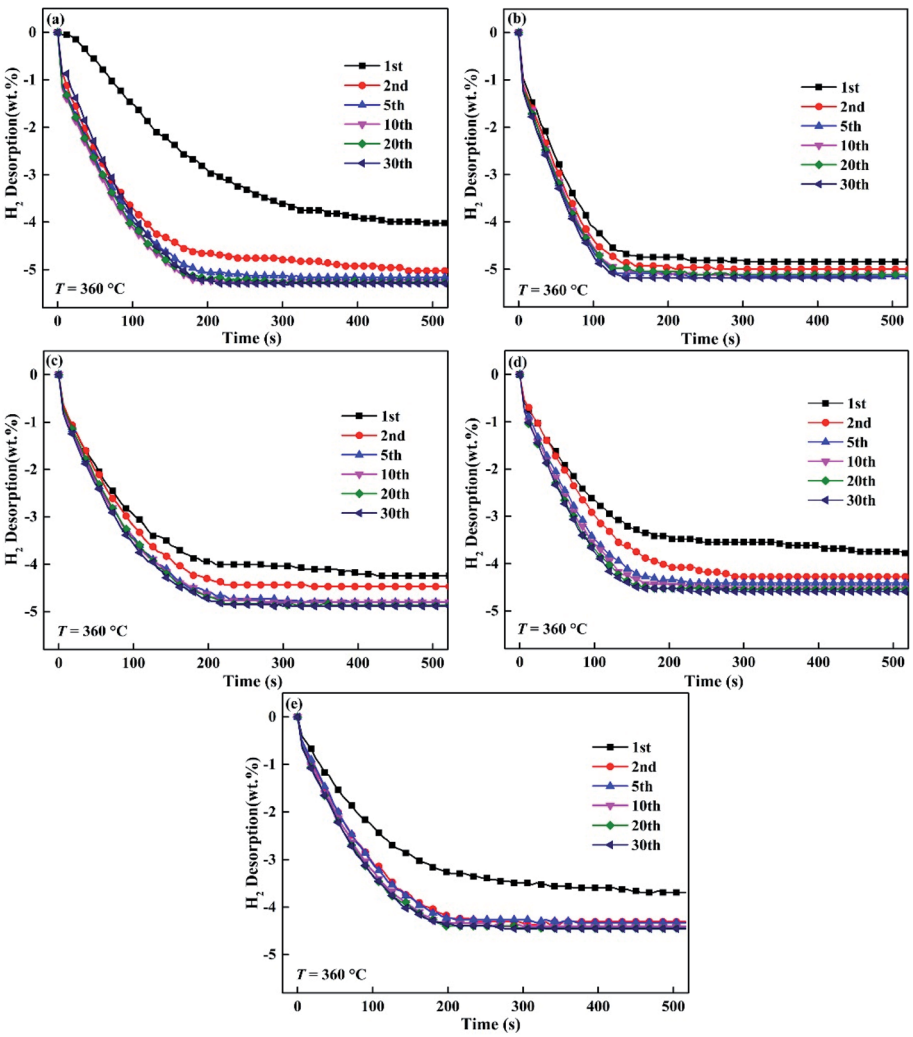

Fig. 7 Dehydrogenation cycling curves of $Mg_{85}Cu_5Ni_{10}$–x wt% TiF_3 (x = 2, 4, 6, 8) alloys at 360 °C: (a) x = 0; (b) x = 2; (c) x = 4; (d) x = 6; (e) x = 8.

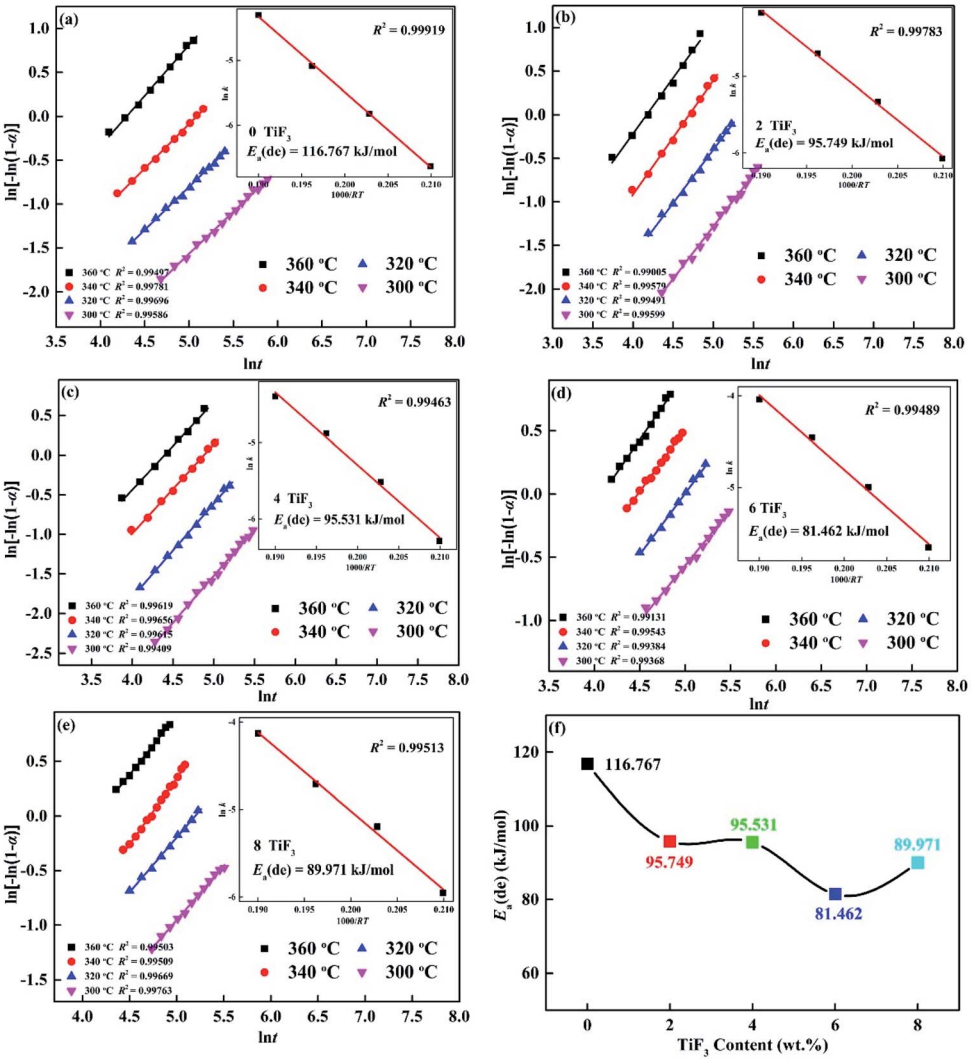

Fig. 8 JMA graphs of $Mg_{85}Cu_5Ni_{10}$ + x wt% TiF_3 (x = 0, 2, 4, 6, 8) alloys different temperatures: (a) x = 0; (b) x = 2; (c) x = 4; (d) x = 6; (e) x = 8 and E_a dehydrogenation (f).

It takes a long time for the five alloys to absorb hydrogen for the first time due to the long process of activating alloys. However, the first dehydrogenation time of $Mg_{85}Cu_5Ni_{10}$–x wt% TiF_3 (x = 2, 4, 6, 8) alloys is shorter than that of $Mg_{85}Cu_5Ni_{10}$–0 wt% TiF_3 indicating that TiF_3 shortens the first dehydrogenation. After the second cycle, the hydrogenation and dehydrogenation rates are obviously accelerated. With the increase of cycle times, the hydrogenation and dehydrogenation rates are gradually improved with good kinetics. The hydrogen absorbing and desorbing cyclic curves are almost identical. It illustrates that the decomposition of TiF_3 does not affect the cyclic stability of the alloys. But it reduces the reversible hydrogen storage capacity. Because the decomposing of TiF_3 and forming of TiH_2/MgF_2 can not react with hydrogen in this condition. Therefore, $Mg_{85}Cu_5Ni_{10}$–x wt% TiF_3 (x = 2, 4, 6, 8) alloys can not reach the theoretical saturated hydrogen storage capacities. The saturated

Table 1 Hydrogen desorption activation energy (E_a(de)), enthalpy change (ΔH) and entropy change (ΔS) of $Mg_{85}Cu_5Ni_{10}$–x wt% TiF_3 (x = 0, 2, 4, 6, 8) alloys and as-cast $Mg_{85}Cu_5Ni_{10}$

$Mg_{85}Cu_5Ni_{10}$–x wt% TiF_3	E_a(de) (kJ mol^{-1})	ΔH_{ab} (kJ mol^{-1})	ΔS_{ab} (J mol^{-1} K^{-1})	ΔH_{de} (kJ mol^{-1})	ΔS_{de} (J mol^{-1} K^{-1})
As-cast $Mg_{85}Cu_5Ni_{10}$ (ref. 27)	119.142	−98.287	−166.292	98.892	165.755
x = 0	116.767	−97.254	−155.682	93.372	151.331
x = 2	95.749	−79.420	−135.903	80.114	134.065
x = 4	95.531	−74.908	−126.432	77.227	129.059
x = 6	81.462	−69.336	−118.058	72.465	121.317
x = 8	89.971	−70.926	−121.503	77.911	131.419

hydrogen storage capacity decreases with the increase of TiF_3 content. On the basis of Fig. 6 and 7, $Mg_{85}Cu_5Ni_{10}$–x wt% TiF_3 (x = 0, 2, 4, 6, 8) alloys still have good hydrogenation and dehydrogenation cyclic stability.

Dehydrogenation activation energy

For further studying the catalytic effect of TiF_3 on the dehydrogenation performance of $Mg_{85}Cu_5Ni_{10}$, we calculated the dehydrogenation activation energy of $Mg_{85}Cu_5Ni_{10}$–x wt% TiF_3 (x = 0, 2, 4, 6, 8) alloys. The dehydrogenation activation energy is a key parameter to describe the dehydriding properties. The kinetic performance of dehydriding evolution is mainly determined by the energy barrier required by MgH_2 changing to Mg by releasing H_2. The dehydrogenation activation energy is the total energy needed to overcome. In general, the kinetic curve of dehydrogenation is fitted by JMA model, and the dehydrogenation activation energy E_a(de) can be calculated by Arrhenius method. Johnson–Mehl–Avrami (JMA) model is expressed by following equation:[33–35]

$$\ln[-\ln(1-\alpha)] = \eta \ln k + \eta \ln t \quad (1)$$

in this equation, α means the reaction fraction at time t, η represents the Avrami exponent reaction order and k indicates an effective kinetic parameter. Fig. 8 describes JMA curves of ln $[-\ln(1-\alpha)]$ *vs.* ln t at different temperatures. The fitting line of JMA curve is almost linear, which illustrates that the dehydriding follows a three-dimensional growth process of

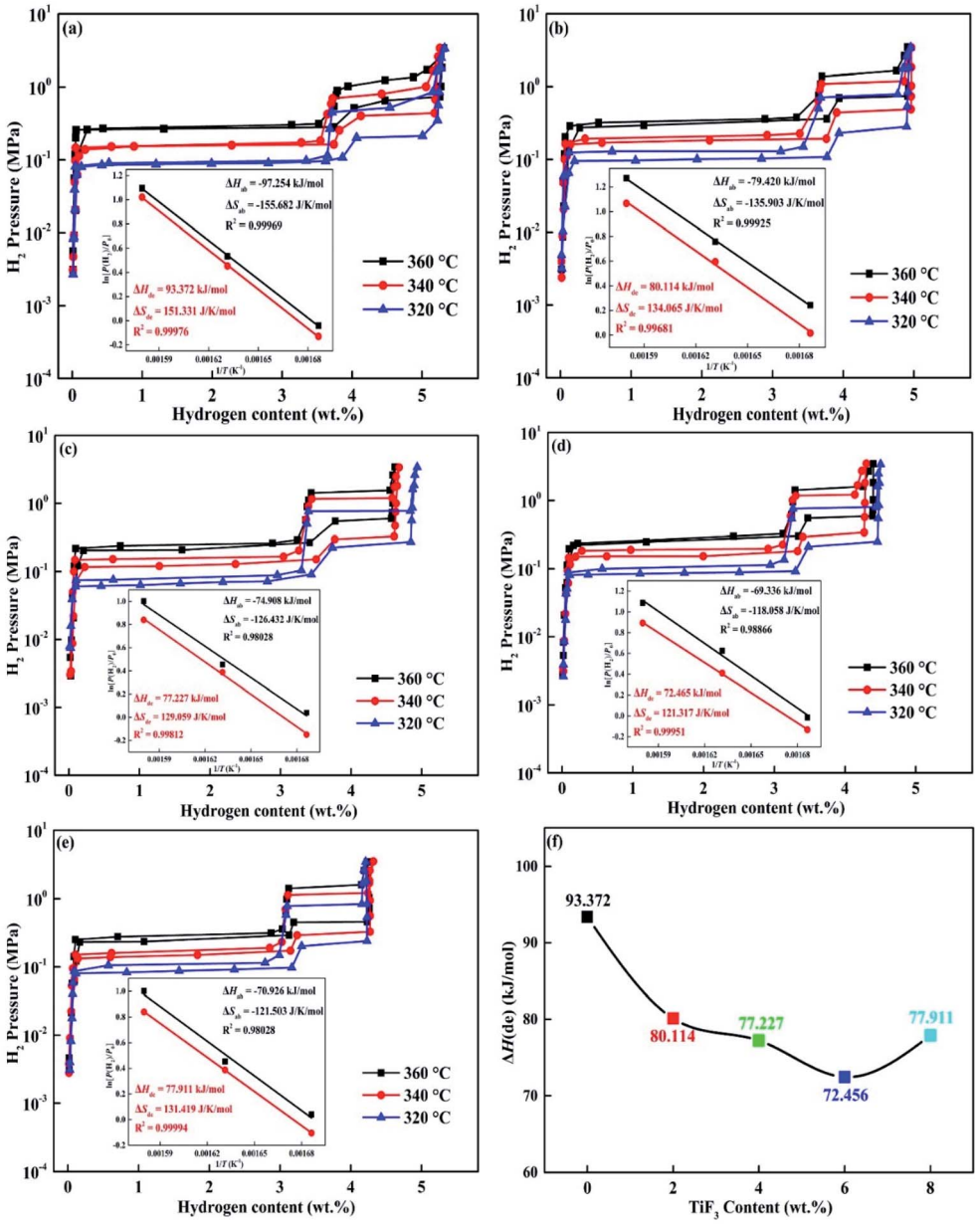

Fig. 9 PCT curves and corresponding van't Hoff plots of $Mg_{85}Cu_5Ni_{10}$ + x wt% TiF_3 (x = 0, 2, 4, 6, 8) alloys different temperatures: (a) x = 0; (b) x = 2; (c) x = 4; (d) x = 6; (e) x = 8 and enthalpy change (ΔH) of dehydrogenation (f).

instantaneous nucleation followed by interface control. The values of η and $\eta \ln k$ express the slope and intercept of JMA curve, from which the value of rate constant k can be determined. As a result, the dehydrogenation activation energy (E_a) can be calculated based on Arrhenius equation:[36,37]

$$k = A \exp[-E_a/RT] \quad (2)$$

in this equation, A is a temperature independent coefficient, T represents the absolute temperature and R means universal gas constant. Fig. 8 also shows the Arrhenius plots and dehydrogenation activation energy E_a(de) of $Mg_{85}Cu_5Ni_{10}$–x wt% TiF_3 (x = 0, 2, 4, 6, 8) alloys. The dehydrogenation activation energy E_a(de) of $Mg_{85}Cu_5Ni_{10}$–x wt% TiF_3 (x = 0, 2, 4, 6, 8) alloys are 116.767, 95.749, 95.531, 81.462 and 89.971 kJ mol^{-1} respectively listed in Table 1. As a comparison, the dehydrogenation activation energy of MgH_2 is 160 kJ mol^{-1}. In our previous study,[27] the dehydrogenation activation energy of as-cast $Mg_{85}Cu_5Ni_{10}$ was 119.142 kJ mol^{-1}, and the E_a(de) of $Mg_{85}Cu_5Ni_{10}$–x wt% CeO_2 (x = 0, 4, 8) alloys were 116.767, 84.824, and 81.211 kJ mol^{-1} respectively. According to the results above, TiF_3 can decrease the dehydrogenation activation energy of $Mg_{85}Cu_5Ni_{10}$ obviously. But there is a point worth noting, the dehydrogenation activation energy E_a(de) of $Mg_{85}Cu_5Ni_{10}$–x wt% TiF_3 (x = 0, 2, 4, 6, 8) alloys decreases first and then increases with the increase of TiF_3 content. This may be due to the increase of TiF_3 content, which leads to the increase of TiH_2 and MgF_2 contents, which cover the surface of the alloys, thus affecting the dehydriding evolution performance. In conclusion, TiF_3 can significantly reduce the dehydrogenation activation energy E_a(de) and ameliorate the kinetic performance of $Mg_{85}Cu_5Ni_{10}$.

Hydrogen storage thermodynamics

For investigating the hydrogen storage thermodynamics of $Mg_{85}Cu_5Ni_{10}$–x wt% TiF_3 (x = 0, 2, 4, 6, 8) alloys, the PCT curves were measured at 360, 340 and 320 °C shown in Fig. 9. All the five alloys almost absorb no hydrogen before reaching the platform pressure due to the front of each PCT curve is almost linear rise. When it reaches the plateau pressure with pressure increasing, the alloy begins to absorb a lot of hydrogen, and the first hydrogen absorption platform is formed. This platform belongs to Mg/MgH_2 hydriding. With the continuous increase of hydrogen pressure, the amount of hydrogen absorption also increases slowly, and then a second hydrogen absorption platform appears which belongs to Mg_2Ni/Mg_2NiH_4 hydriding. After that, the alloy reaches the saturated state with hydrogen pressure increasing. The dehydriding evolution is the opposite with the decrease of hydrogen pressure. Here we only discuss the pressure of the first platform pressure belonging to Mg/MgH_2. According to the pressure value of platform pressure at different temperatures, the enthalpy change (ΔH) and entropy change (ΔS) can be calculated by the van't Hoff equation:[38]

$$\ln[P(H_2)/P_0] = \Delta H/(RT) - \Delta S/R \quad (3)$$

in this equation, $P(H_2)$ is the equilibrium hydrogen gas pressure, P_0 means the standard atmospheric pressure, T represents the sample temperature and R expresses the gas constant, respectively. The van't Hoff plots, ΔH and ΔS are also shown in the inserted graphs in Fig. 9. On the basis of Fig. 9(f), the ΔH(de) of $Mg_{85}Cu_5Ni_{10}$–x wt% TiF_3 (x = 0, 2, 4, 6, 8) alloys is 93.372, 80.114, 77.227, 72.456 and 77.911 kJ mol^{-1} respectively shown in Table 1. For comparison, the ΔH(de) of as-cast $Mg_{85}Cu_5Ni_{10}$ was 98.892 kJ mol^{-1} and the ΔH(de) of $Mg_{85}Cu_5Ni_{10}$–x wt% CeO_2 (x = 0, 4, 8) alloys were 92.441, 79.548, and 80.018 kJ mol^{-1} respectively.[27] The ΔH(de) values of TiF_3 catalyzed alloys are lower than that of as-cast $Mg_{85}Cu_5Ni_{10}$ alloy and $Mg_{85}Cu_5Ni_{10}$–0 wt% TiF_3 illustrating that thermodynamic stability of the alloys decrease. Although TiF_3 is decomposed into TiH_2 and MgF_2 during the hydrogen absorption and desorption cycles, some defects, grain boundaries and nano interfaces are also added. Because the bond energy of Mg–H bond at the grain boundary is relatively low, the thermodynamic properties of the alloys are improved.

Conclusions

$Mg_{85}Cu_5Ni_{10}$–x wt% TiF_3 (x = 0, 2, 4, 6, 8) alloys were prepared *via* ball milling. The compounds contained Mg, Mg_2Ni, Mg_2Cu and TiF_3. The alloys catalyzed by TiF_3 have faster hydriding/dehydriding kinetics and lower thermodynamic stability, even though TiF_3 decomposes into TiH_2 and MgF_2 during hydriding and dehydriding. TiF_3, TiH_2 and MgF_2 promote to forming crystal defects, dislocations, grain boundaries and nanocrystals which have a positive effect on accelerating the rate of hydrogen absorption and desorption. The dehydrogenation activation energy E_a(de) and dehydrogenation enthalpy ΔH(de) are reduced to 81.462 from 116.767 kJ mol^{-1} and 72.456 from 93.372 kJ mol^{-1} respectively by 6 wt% TiF_3. An appropriate amount of TiF_3 can improve the kinetics and thermodynamics of hydrogen absorption and desorption of $Mg_{85}Cu_5Ni_{10}$.

Conflicts of interest

There are no conflicts to declare.

Acknowledgements

This work is financially supported by the National Natural Science Foundations of China (51901105 and 51871125), Natural Science Foundation of Inner Mongolia, China (No. 2019BS05005), and Inner Mongolia University of Science and Technology Innovation Fund (2019QDL-B11).

References

1 K. Manickam, P. Mistry, G. Walker, D. Grant, C. E. Buckley, T. D. Humphries, M. Paskevicius, T. Jensen, R. Albert, K. Peinecke and M. Felderhoff, *Int. J. Hydrogen Energy*, 2019, **44**, 7738–7745.
2 J. J. Liu, H. H. Cheng, S. M. Han, H. F. Liu and J. Huot, *Energy*, 2020, **192**, 116617.
3 C. Milanese, T. R. Jensen, B. C. Hauback, C. Pistidda, M. Dornheim, H. Yang, L. Lombardo, A. Zuettel,

Y. Filinchuk, P. Ngene, P. E. de Jongh, C. E. Buckley, E. M. Dematteis and M. Baricco, *Int. J. Hydrogen Energy*, 2019, **44**, 7760–7774.
4 S. Yasuoka, J. Ishida, K. Kishida and H. Inui, *J. Power Sources*, 2017, **346**, 56–62.
5 Y. H. Zhang, M. Ji, Z. M. Yuan, W. G. Bu, Y. Qi and S. H. Guo, *RSC Adv.*, 2017, **7**, 37689–37698.
6 X. Y. Chen, R. R. Chen, X. Ding, H. Z. Fang, X. Z. Li, H. S. Ding, Y. Q. Su, J. J. Guo and H. Z. Fu, *Energy*, 2019, **166**, 587–597.
7 N. A. A. Majid, N. Maeda and M. Notomi, *Int. J. Hydrogen Energy*, 2019, **44**, 29189–29195.
8 B. Galey, A. Auroux, S. S. Etienne, M. Grellier, S. Dhaher and G. Postole, *Sustainable Energy Fuels*, 2018, **2**, 2335–2344.
9 F. A. H. Yap, N. N. Sulaiman and M. Ismail, *Int. J. Hydrogen Energy*, 2019, **44**, 30583–30590.
10 V. A. Yartys, M. Baricco, J. B. von Colbe, D. Blanchard and C. Zlotea, *Int. J. Hydrogen Energy*, 2019, **44**, 7809–7859.
11 B. X. Dong, H. Tian, Y. C. Wu, F. Y. Bu, W. L. Liu and Y. L. Teng, *Int. J. Hydrogen Energy*, 2016, **41**, 14507–14518.
12 Y. Yin, B. Li, Z. M. Yuan, Y. Qi and Y. H. Zhang, *RSC Adv.*, 2018, **8**, 34525–34535.
13 İ. Muz and M. Atiş, *J. Alloys Compd.*, 2016, **667**, 275–281.
14 Q. Luo, J. D. Li, B. Li, B. Liu, H. Y. Shao and Q. Li, *J. Magnesium Alloys*, 2019, **7**, 58–71.
15 N. Lobo, A. Takasaki, K. Mineo, A. Klimkowicz and K. Goc, *Int. J. Hydrogen Energy*, 2019, **44**, 29179–29188.
16 K. Kitabayashi, K. Edalati, H. W. Li, E. Akiba and Z. J. Horita, *Adv. Energy Mater.*, 2020, **22**, 1900027.
17 S. C. Gao, X. H. Wang, H. Z. Liu, T. He, Y. Y. Wang, S. Q. Li and M. Yan, *J. Power Sources*, 2019, **438**, 227006.
18 J. Li, B. Li, H. Shao, W. Li and H. Lin, *Catalyst*, 2018, **8**, 89.
19 H. Zhang, X. Zheng, X. Tian, Y. Liu and X. Li, *Prog. Nat. Sci.: Mater. Int.*, 2017, **27**, 50–57.
20 K. Alsabawi, A. Mac, E. Gray and C. J. Webb, *Int. J. Hydrogen Energy*, 2019, **44**, 2976–2980.
21 M. M. Hu, X. B. Xie, M. Chen, C. X. Zhu and T. Liu, *J. Alloys Compd.*, 2020, **817**, 152813.
22 M. Ismail, Y. F. A. Halim, N. N. Sulaiman and M. H. I. Ishak, *J. Alloys Compd.*, 2016, **678**, 297–303.
23 Z. M. Yuan, B. W. Zhang, Y. H. Zhang, S. H. Guo, X. P. Dong and D. L. Zhao, *J. Mater. Sci. Technol.*, 2018, **34**, 1851–1858.
24 Z. M. Yuan, W. Zhang, P. L. Zhang, Y. H. Zhang, W. G. Bu, S. H. Guo and D. L. Zhao, *RSC Adv.*, 2017, **7**, 56365–56374.
25 Y. H. Zhang, W. Zhang, J. L. Gao, Z. M. Yuan, W. G. Bu and Y. Qi, *Acta Metall. Sin.*, 2017, **11**, 10–18.
26 Y. H. Zhang, M. Ji, Z. M. Yuan, J. L. Gao, Y. Qi, X. P. Dong and S. H. Guo, *J. Rare Earths*, 2018, **36**, 409–417.
27 Y. Yin, B. Li, Z. M. Yuan, Y. Qi and Y. H. Zhang, *J. Rare Earths*, 2020, **38**, 983–993.
28 Z. M. Yuan, T. Yang, W. G. Bu, H. W. Shang, Y. Qi and Y. H. Zhang, *Int. J. Hydrogen Energy*, 2016, **41**, 5994–6003.
29 T. Liu, T. W. Zhang, X. Z. Zhang and X. G. Li, *Int. J. Hydrogen Energy*, 2011, **36**, 3515–3520.
30 Y. H. Zhang, T. Yang, W. G. Bu, Y. Cai, G. F. Zhang and D. L. Zhao, *Trans. Nonferrous Met. Soc. China*, 2013, **23**, 3668–3676.
31 N. S. Mustafa and M. Ismail, *Int. J. Hydrogen Energy*, 2019, **44**, 21979–21987.
32 N. N. Sulaiman and M. Ismail, *Int. J. Hydrogen Energy*, 2019, **44**, 30574–30582.
33 M. Pourabdoli, S. Raygan, H. Abdizadeh and D. Uner, *Int. J. Hydrogen Energy*, 2013, **38**, 11910–11919.
34 G. Barkhordarian, T. Klassen and R. Bormann, *J. Alloys Compd.*, 2006, **407**, 249–255.
35 L. J. Wei, H. Gu, Y. F. Zhu and L. Q. Li, *Int. J. Hydrogen Energy*, 2012, **37**, 17146–17152.
36 T. Liu, Y. R. Cao, C. G. Qin, W. S. Chou and X. G. Li, *J. Power Sources*, 2014, **246**, 277–282.
37 T. Kimura, H. Miyaoka, T. Ichikawa and Y. Kojima, *Int. J. Hydrogen Energy*, 2013, **38**, 13728–13733.
38 H. Falahati and D. P. J. Barz, *J. Hydrogen Energy*, 2013, **38**, 8838–8851.